CrossMark

An innovative hardware in the loop architecture for the analysis of railway braking under degraded adhesion conditions through roller-rigs

R. Conti, E. Meli *, A. Ridolfi, A. Rindi

University of Florence, Department of Industrial Engineering, Italy

ARTICLE INFO

ABSTRACT

Nowadays, the longitudinal train dynamical behaviour is almost totally controlled by braking on board subsystems, such as Wheel Slide Protection (WSP) devices. The study and the development of these systems are fundamental for the vehicle safety, especially at high speeds and under degraded adhesion conditions. Traditionally, the performance of braking subsystems is tested on full-scale roller-rigs, to save time and to avoid expensive on-track tests. However, the study of the subsystem behaviour under degraded adhesion conditions on roller-rigs is still limited to few applications since high slidings among rollers and wheelsets generate wear of the rolling surfaces. This event is not acceptable because of the effects on the maintenance costs (the rollers have to be turned or substituted), on the system dynamical stability and on the safety.

In this work the authors present an innovative Hardware In the Loop (HIL) approach for testing braking on board subsystems on full-scale roller-rigs. The new approach permits the reproduction on the roller-rig of a generic wheel-rail adhesion pattern and, in particular, of degraded adhesion conditions. The described strategy is the same implemented on the innovative full-scale roller-rig, recently built by Trenitalia and owned by SIMPRO, in the Railway Research and Approval Center of Firenze-Osmannoro (Italy). To validate the proposed approach, a complete model of the HIL system has been developed; the results provided by the simulation model have been compared to the experimental data provided by Trenitalia and relative to the on-track tests performed in Velim, Czech Republic, with a UIC-Z1 coach equipped with a fully-working WSP system. The complete model is based on the real characteristics of the components provided by Trenitalia. The preliminary validation performed with the HIL model highlighted the good performance of the HIL strategy in reproducing on the roller-rig the complex behaviour of the degraded adhesion during the braking of a railway vehicle. The next steps of the research activity will be the implementation both of the controller and the virtual vehicle model on the real Firenze-Osmannoro roller-rig.

© 2014 Elsevier Ltd. All rights reserved.

1. Introduction

Currently, on board subsystems, such as Wheel Slide Protection (WSP) braking devices, almost totally control the longitudinal train dynamics. The vehicle safety requires an accurate study of the system performances, especially at high speeds and under degraded adhesion conditions. On-track tests are usually quite expensive in terms of infrastructure and vehicle management. To reduce these costs, the performances of braking subsystems are traditionally investigated by means of full-scale roller-rigs [1–4]. Nevertheless, in case of degraded adhesion, the use of roller-rigs is still limited to few applications (full-scale roller-rigs for the study of the wear [5], HIL systems for WSP tests [16,20] and full-scale roller-rigs for

locomotive tests [7,16,20]), since high slidings between rollers and wheelsets produce wear of the rolling surfaces. The wear of the flange can lead to the vehicle derailment, while the wear of the tread can produce hunting instability of the vehicle [6,8,24]. The wheel flat may also generate unsafe vibrations of the vehicle on the roller-rig. This scenario is not acceptable because of the effects on the maintenance costs (the rollers have to be turned or substituted), on the system dynamical stability and on safety.

In this paper the authors present an innovative Hardware In the Loop (HIL) approach for testing braking on board subsystems on full-scale roller-rigs. The new approach permits the reproduction on the roller-rig of a generic wheel-rail adhesion pattern and, in particular, of degraded adhesion conditions (as defined in [9], a typical degraded adhesion coefficient is less than 0.10). More in detail, a simulation of mechanical impedance is performed: the roller motors are controlled in order to recreate, on the wheelsets, the

* Corresponding author. Tel.: +39 055 4796286; fax: +39 055 4796342.
E-mail address: enrico.meli@unifi.it (E. Meli).

same angular velocities, applied torques and tangential efforts (exchanged between the wheelsets and the rails) calculated by a reference virtual railway vehicle model. Since the real adhesion coefficient between the rollers and the wheelsets is far higher than the simulated one, negligible sliding occurs between them.

The described strategy has been simulated in the Matlab-Simulink environment [10] through a model of the whole HIL architecture in which each component is modelled according to the real characteristics provided by Trenitalia. The proposed approach has been validated through a comparison with the experimental data provided by Trenitalia and relative to on-track tests performed on a straight railway track (in Velim, Czech Republic) with a UIC-Z1 coach equipped with a fully-working WSP system [11–13]. The research paper is organised as follows: the introduction describes both the state of art of the roller-rigs and the innovative contributions of this work; in the chapters concerning the general architecture and the modelling of the Firenze-Osmannoro roller-rig, the authors present the main model parts of the whole architecture and the interactions among them. Finally, in the experimental data and model validation chapters, the data used as validation, and the numerical simulations are compared.

2. General architecture of the HIL system

In this chapter the innovative architecture of the Firenze-Osmannoro HIL system is briefly described. Fig. 1 schematically shows the main parts of the architecture (both for the hardware components and the software ones). The models used to simulate all these parts will be better explained in Section 3.

The architecture comprises four main elements:

- the *test-rig (hardware)*, composed of two main parts: the UIC-Z1 railway vehicle (equipped with the WSP system) [11,12] and the Firenze-Osmannoro roller-rig (with the innovative actuation system developed in collaboration with SICME and based on IPM synchronous motor with high performance characteristics which will be better explained in Section 3.1.3.1) [14,15].

The inputs of the test-rig are the roller control torques while the outputs are the longitudinal reaction forces measured on the roller supports and the measured angular velocities of the rollers;

- the *virtual railway vehicle model (software)*, representing the model used to simulate the vehicle behaviour on the rails under different adhesion conditions [16,20] and designed for a real-time implementation. This 2D multibody model simulates the longitudinal dynamics of the vehicle while an innovative 2D adhesion model especially developed [16,17] to accurately reproduce the real behaviour of the adhesion coefficient during braking phases under degraded adhesion conditions. The inputs are the estimated torques on the wheelsets and the outputs are the simulated wheelset angular velocities and the tangential contact forces on the wheelsets;

- the *innovative controllers (software)* reproduce on the roller-rig the same dynamical behaviour of the virtual train model (through the roller control torques) in terms of wheelset angular velocities, applied torques and, consequently, tangential forces [8]. Due to the HIL system non-linearities, a sliding mode approach has been adopted for the controllers [18,19];

- the *torque estimators (software)*: the data measured by the sensors installed on the roller-rig are only the roller angular velocities and the longitudinal reaction forces on the roller supports. No sensors will be placed on the vehicle to speed up the set up process. Starting from these quantities, this block estimates the torques applied on the wheelsets.

3. Modelling of the Firenze-Osmannoro HIL system

In this section the models of the HIL system presented in the previous section (both hardware and software parts) and of all the components of the HIL architecture will be explained in detail. The main elements of the architecture are the same of Fig. 1, but, in this case, the test-rig is completely simulated both for the UIC-Z1 railway vehicle (3D vehicle model and WSP model) and for the roller-rig (roller-rig 3D model). An innovative 3D contact model
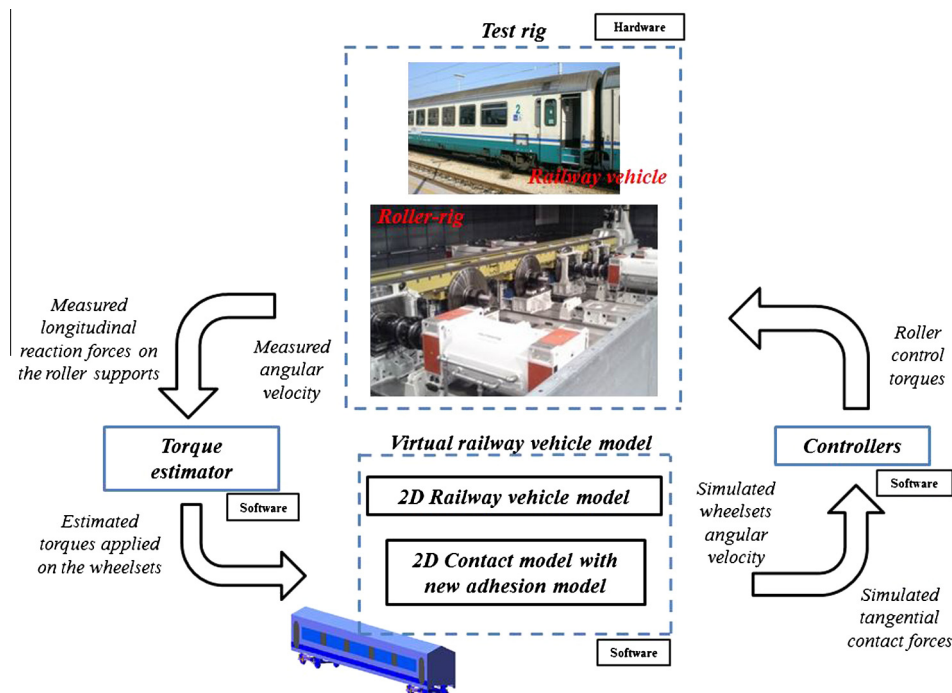

Fig. 1. General architecture of the HIL system.

especially developed by the authors for this kind of application is used [20–22]. The mechanical and electrical characteristics of the vehicle [11,12] and of the roller-rig [14,15] are directly provided by Trenitalia and RFI.

The flow of the data among the model parts is shown in Fig. 2.

3.1. The test-rig model

The inputs of the whole test-rig model are the 8 roller control torques u^l, u^r (left and right) evaluated by the controllers to reproduce on the test-rig the same dynamical behaviour of the virtual railway model. The outputs are the 8 roller angular velocities ω_r^l, ω_r^r and the longitudinal reaction forces T_{mis}^l, T_{mis}^r measured on the roller supports. The test-rig model is composed of four parts (Fig. 2):

3.1.1. The vehicle model

The considered railway vehicle is the UIC-Z1 coach (shown in Fig. 3); its geometrical and physical characteristics are provided by Trenitalia [11]. The wagon consists of one carbody, two bogie frames, eight axleboxes and four wheelsets. The UIC-Z1 coach has a two-stage suspension system: the primary suspension, including springs, dampers and axlebox bushings, connects the bogie frames to the four axleboxes while the secondary suspension, including springs, dampers, lateral bump-stops, anti-roll bar and traction rod, connects the carbody to the bogie frames. The multibody vehicle model takes into account all the degrees of freedom (DOFs) of system bodies. Both the primary suspensions and the secondary ones have been modelled through 3D visco-elastic force elements able to describe all the main non-linearities of the system.

The inputs of the model are the 4 wheelset torques C_s modulated by the on board WSP and the contact forces calculated by the contact model, while the outputs are the kinematic wheelset variables transmitted to the contact model, the 4 original torques C (without the on board WSP modulation) and the 4 wheelset angular velocities ω_w. These last two outputs are not accessible by the HIL system.

3.1.2. The wheel slide protection system model

The WSP device installed on the UIC-Z1 coach [12,17] allows the control of the torques applied to the wheelsets, to prevent macro-sliding during the braking phase.

Fig. 3. UIC-Z1 coach.

In Fig. 4 the logical scheme and an image of the WSP device are shown. The inputs are the braking torques C and the wheelset velocities ω_w, while the outputs are the modulated braking torques C_s. The WSP system working principle can be divided into three different tasks: the evaluation of the reference vehicle velocity V_{ref} and acceleration a_{ref} based on the wheelset angular velocities ω_w and accelerations $\dot{\omega}_w$; the computation of the logical sliding state $state_{WSP}$ (equal to 1 if sliding occurs and 0 otherwise) and the consequent torque modulation, through a speed and an accelerometric criterion and by means of a suitable logical table [17]; the periodic braking release to bring back the perceived adhesion coefficient to the original value (often used when degraded adhesion conditions are very persistent and the WSP logic tends to drift).

3.1.3. The roller-rig model

The 3D multibody model of the roller-rig (see Fig. 5 and Table 1) consists of 8 independent rollers with a particular roller profile able to exactly reproduce the UIC60 rail pattern with different laying angles α_p [14]. The railway vehicle is axially constrained on the rollers using two axial links (front and rear) modelled by means of 3D force elements with linear stiffness and damping. The inputs of the test-rig model are the 8 torques u^l, u^r evaluated by the controllers and the contact forces calculated by the contact model;
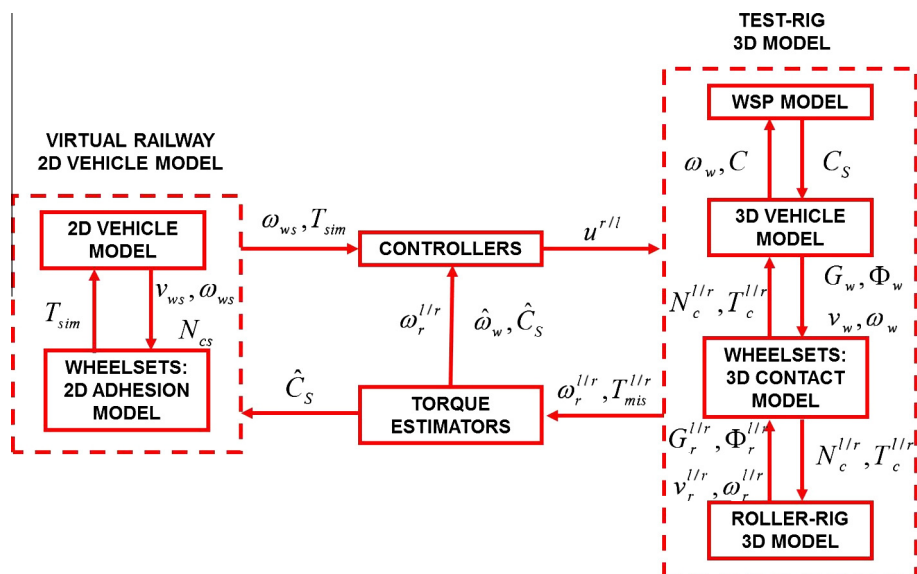

Fig. 2. Interactions among the models of the various HIL architecture components.
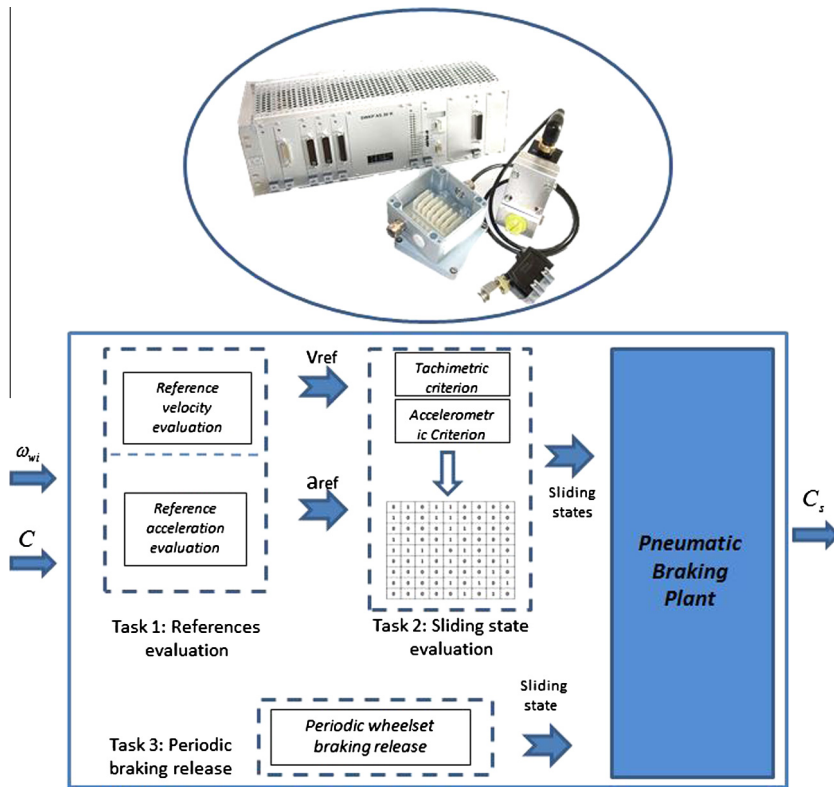
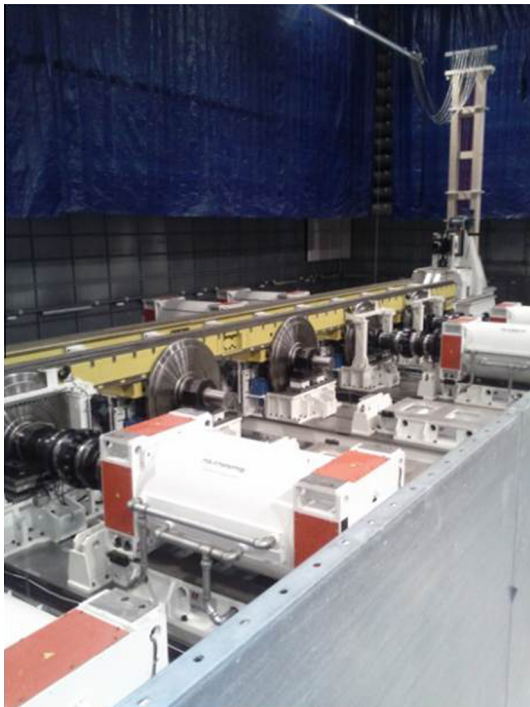**Fig. 4.** WSP device and its logical scheme.

Fig. 5. The right side of roller-rig system with the synchronous motors and the rollers placed in the semi-anechoic room of the Research and Approval Center of Firenze-Osmannoro.

the outputs are the roller angular velocities ω_r^l, ω_r^r, the longitudinal reaction forces T_{mis}^l, T_{mis}^r measured on the roller supports and the kinematic wheelset variables transmitted to the contact model.

Table 1
Main characteristics of the roller-rig system and of the wheelsets.

Parameter	Units	Value
Roller radius r_r	m	0.725
Roller mass m_r	kg	2980
Roller inertia J_r	kg m^2	705
Wheelset radius r_w	m	0.445
Wheelset mass m_w	kg	1300
Wheelset inertia J_w	kg m^2	160

The roller-rig actuation system consists of 8 synchronous motors, especially designed and developed in cooperation with SICME [15] for this kind of application (see Table 2). The HIL architecture includes a direct-drive connection between the roller and the electrical machine. The synchronous motors have high efficiency associated with high torque density and flux weakening capability. Furthermore, to reach the dynamical and robustness performances required by the railway full-scale roller-rig, the motors are designed with a multilayer-rotor characterised by a high saliency ratio ξ and Interior Permanent Magnets (IPM). The IPM motors are controlled in real-time through vector control techniques; more particularly the vector control is a torque-controlled drive system in which the controller follows a desired torque [15,25–28].

3.1.3.1. IPM synchronous motors. The motor is composed of a rotor (representing the part rigidly connected to the rotating shaft), in which there are P magnetic poles of alternating polarity made by Permanent Magnets (PM), and a stator, in which all the windings of the power supply circuit are present. The stator poles create a rotating magnetic field which drags the magnets of the rotor part. For reasons of simplicity, it is useful to carry out the dynamic model of the motor using an equivalent 2-phase motor consisting of two windings, respectively placed on two orthogonal (Figs. 6, 7)
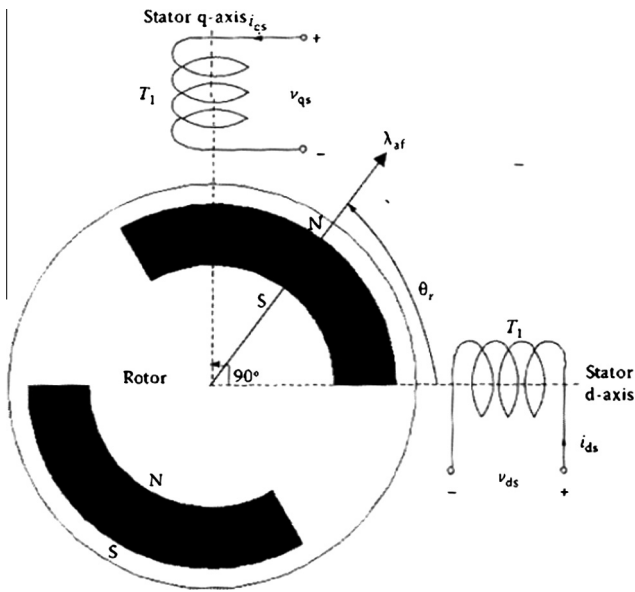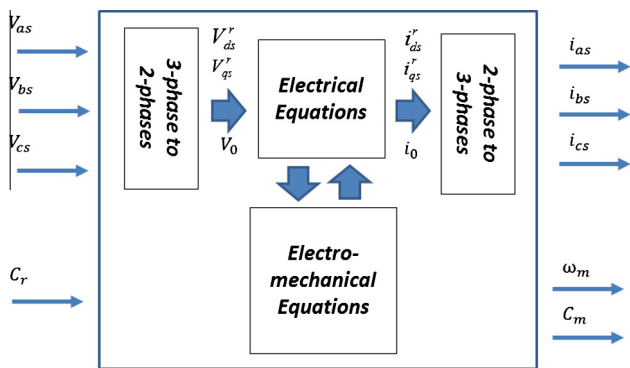
Fig. 6. Two-phase model.

Fig. 7. Inputs and outputs of the IPM synchronous motor model.

Table 2
IPM synchronous motor characteristics.

Parameter	Units	Value
Nominal torque T_b	Nm	38,500
Maximum speed ω_{max}	rad/s	141
Motor inertia J_{mot}	kg m^2	200
Mutual flux linkages amplitude $\|\lambda_\mathbf{m}\|$	Wb	3.926
Inductance on the q-axis L_q	μH	326
Inductance on the d-axis L_d	mH	1.8
Stator resistance R_s	mΩ	15.9
Rotor resistance R_r	mΩ	15.9
Number of poles P	–	6
Maximum torque angle $\sin \delta_{max}$	–	0.39
Maximum stator current $\|\mathbf{i}_s^{max}\|$	A	1500
Saliency ratio $\tilde{\xi}$	–	5.6
Viscous friction coefficient B_{mot}	Nm s/rad	14.7

directions (the direct axis d and the quadrature axis q). At this point, it is possible to create a motor model in which all the physical parameters are referred to the stator or to the rotor: the first approach has the disadvantage that the stator winding inductances depend on the rotor position, while in the second one the inductances are constants. In order to obtain constant inductances, it is necessary to transform the stator windings, fixed in the space, into fictitious windings which rotate at the rotor electric speed. Finally the transformation between 2-phase model and 3-phase

model is introduced simplify the development of the motor control (see Eqs. (6) and (7)).

The electrical equations referred to the rotor frame of the IPM synchronous motor are the following:

$$\begin{bmatrix} v_{qs}^r \\ v_{ds}^r \end{bmatrix} = [L_{qd}] \begin{bmatrix} i_{qs}^r \\ i_{ds}^r \end{bmatrix} + \begin{bmatrix} \omega_r \|\lambda_\mathbf{af}\| \\ 0 \end{bmatrix} \tag{1}$$

with

$$[L_{qd}] = \begin{bmatrix} R_s + \frac{d}{dt}L_q & \omega_r L_d \\ -\omega_r L_q & R_s + \frac{d}{dt}L_d \end{bmatrix} \tag{2}$$

where $\mathbf{v}_\mathbf{qds}^\mathbf{r} = [v_{qs}, v_{ds}]^T$ is the winding voltage vector on the fictitious rotating stator, L_{qd} is the inductance matrix (the rotor and stator resistances R_r, R_s and the inductances L_q, L_d are provided by the motor constructor), $\mathbf{i}_\mathbf{qds}^\mathbf{r} = [i_{qs}, i_{ds}]^T$ is the stator current vector referred to the rotor frame and $[\omega_r\|\lambda_\mathbf{af}\|, 0]^T$ is an additional component due to the rotation of the Permanent Magnets on the rotor ($\omega_r = \dot{\theta}_r$ is the rotor angular speed and $\|\lambda_\mathbf{af}\|$ is the amplitude of the armature flux linkage vector $\lambda_\mathbf{af}$ due to the rotor magnets). The electro-mechanical equations used to couple Eq. (1) with the mechanical part are:

$$T_e = \frac{3}{2}\frac{P}{2}\left[\|\lambda_\mathbf{af}\| + (L_d + L_q)i_{ds}^r\right]i_{qs}^r \tag{3}$$

$$J_{mot}\dot{\omega}_m + B_{mot}\omega_m = T_e - C_r \tag{4}$$

where T_e is the electric torque, P is the pole number, ω_m is the motor angular speed, J_{mot} is the motor inertia, B_{mot} is the viscous friction and C_r is the load torque; this way the complete electro-mechanical model of the motor is completed. As it can be seen, the electric torque T_e is a function of the currents flowing inside the windings, while the rotor speed $\omega_r = \dot{\theta}_r$ is a function of the motor speed ω_m and the mechanical efficiency η_{mech}:

$$\omega_m = \frac{\eta_{mech}}{P}\omega_r. \tag{5}$$

The transformation between the 2-phase model and the 3-phase one is given by:

$$\begin{bmatrix} i_{qs}^r \\ i_{ds}^r \\ i_0 \end{bmatrix} = \frac{2}{3}\begin{bmatrix} \cos\theta_r & \cos\left(\theta_r - \frac{2\pi}{3}\right) & \cos\left(\theta_r + \frac{2\pi}{3}\right) \\ \sin\theta_r & \sin\left(\theta_r - \frac{2\pi}{3}\right) & \sin\left(\theta_r + \frac{2\pi}{3}\right) \\ \frac{1}{2} & \frac{1}{2} & \frac{1}{2} \end{bmatrix}\begin{bmatrix} i_{as} \\ i_{bs} \\ i_{cs} \end{bmatrix} \tag{6}$$

where $\mathbf{i}_\mathbf{qd0}^\mathbf{r} = [i_{qs}, i_{ds}, i_0]^T$ is the stator current in the 2-phase model, i_0 is a fictitious current used for the transformation, θ_r is the rotor angular position with respect to the d–q frame and $\mathbf{i}_\mathbf{abc}^\mathbf{r} = [i_{as}, i_{bs}, i_{cs}]^T$ is the stator current in the 3-phase model. The voltage transformation between the 3-phase model and the 2-phase one is defined as:

$$\begin{bmatrix} V_{as} \\ V_{bs} \\ V_{cs} \end{bmatrix} = \begin{bmatrix} \cos\theta_r & \sin\theta_r & 1 \\ \cos\left(\theta_r - \frac{2\pi}{3}\right) & \sin\left(\theta_r - \frac{2\pi}{3}\right) & 1 \\ \cos\left(\theta_r + \frac{2\pi}{3}\right) & \sin\left(\theta_r + \frac{2\pi}{3}\right) & 1 \end{bmatrix}\begin{bmatrix} V_{ds}^r \\ V_{qs}^r \\ V_0 \end{bmatrix} \tag{7}$$

where $\mathbf{V}_\mathbf{abc}^\mathbf{r} = [V_{as}, V_{bs}, V_{cs}]^T$ is the stator voltage in the 3-phase model, V_0 is a fictitious voltage used for the transformation and $\mathbf{V}_\mathbf{qd0}^\mathbf{r} = [V_{qs}, V_{ds}, V_0]^T$ is the stator voltage in the 2-phase model. The following scheme describes the inputs and the outputs of the IPM synchronous motor model based on Eqs. (1), (3), (6) and (7).

3.1.3.2. Vector control of the IPM synchronous motors. The vector controls are different techniques which directly control in real-time the motor torque by means of vectorial values of currents and voltages. The vector control employed in this case is the torque-controlled drive system in which the controller follows a

desired torque T_e^*. The desired 3-phase currents used as inputs of the synchronous machine (see Fig. 8) are defined as:

$$i_{as}^* = \|\mathbf{i_s^*}\| \sin(\omega_r t + \delta^*)$$
$$i_{bs}^* = \|\mathbf{i_s^*}\| \sin\left(\omega_r t + \delta^* - \frac{2\pi}{3}\right)$$
$$i_{cs}^* = \|\mathbf{i_s^*}\| \sin\left(\omega_r t + \delta^* + \frac{2\pi}{3}\right) \qquad (8)$$

where δ^* is the desired reference torque angle (the angle between the armature flux linkages vector due to rotor magnets $\lambda_{\mathbf{af}}$ and the reference of the stator current vector $\mathbf{i_s^*} = [i_{as}^*, i_{bs}^*, i_{cs}^*]^T$). The quantities with the apex '*' are reference variables. The torque-controlled drive system is schematised in Fig. 8.

The inputs of the vector control are the electric torque T_e^* and the amplitude of the mutual flux linkages $\|\lambda_{\mathbf{m}}^*\|$. The outputs are the stator current $\|\mathbf{i_s^*}\|$ and the torque angle δ^* and can be calculated, starting from the inputs, solving the following algebraic system:

$$T_e^* = \frac{3}{2}\frac{P}{2}\left[\|\lambda_{\mathbf{af}}\|\|\mathbf{i_s^*}\|\sin\delta^* + \frac{1}{2}(L_d - L_q)\|\mathbf{i_s^*}\|^2 \sin 2\delta^*\right] \qquad (9)$$

$$\|\lambda_{\mathbf{m}}^*\| = \sqrt{(\|\lambda_{\mathbf{af}}\| + L_d\|\mathbf{i_s^*}\|\cos\delta^*)^2 + (L_q\|\mathbf{i_s^*}\|\sin\delta^*)^2} \qquad (10)$$

The inverter model permits to transform the references of the stator current vector $\mathbf{i_s^*} = [i_{as}^*, i_{bs}^*, i_{cs}^*]^T$ into the stator voltage vector $\mathbf{v_s} = [v_{as}, v_{bs}, v_{cs}]^T$ (the inputs of the synchronous motor model). The electro-mechanical IPM synchronous motor characteristics are summarised in Table 2.

3.1.3.3. The roller-rig sensors. The main sensors installed on the roller-rig (see Fig. 9) are the absolute encoders and the 3-axial load cells on the roller supports. These sensors are employed both in the torque estimators and in the controllers and measure, respectively, the roller angular velocities ω_r^l, ω_r^r and the longitudinal reaction forces T_{mis}^l, T_{mis}^r on the roller supports. The sensor characteristics are reported in Table 3 [15].

3.1.4. The wheel-roller contact model

The 3D contact model evaluates the contact forces $\mathbf{N_c^{l/r}}$, $\mathbf{T_c^{l/r}}$ for all the 8 wheel-roller pairs starting from the kinematic variables of the wheelsets and of the rollers: their positions $\mathbf{G_w}$, $\mathbf{G_r^{l/r}}$, orientations $\mathbf{\Phi_w}$, $\mathbf{\Phi_r^{l/r}}$, velocities $\mathbf{v_w}$, $\mathbf{v_r^{l/r}}$ and angular velocities $\omega_{\mathbf{w}}$, $\omega_{\mathbf{r}}^{l/r}$ (see Fig. 10).

The contact model comprises three different steps. Firstly, all the contact points $\mathbf{P_{c^{l/r}}}$ of each wheel-roller pair are detected. Some innovative procedures have been recently developed by the authors [20–22]; the new algorithms are based on the reduction of the algebraic contact problem dimension through exact analytical techniques [23]. Secondly, the normal contact problem is solved through the Hertz theory [29] to evaluate the normal
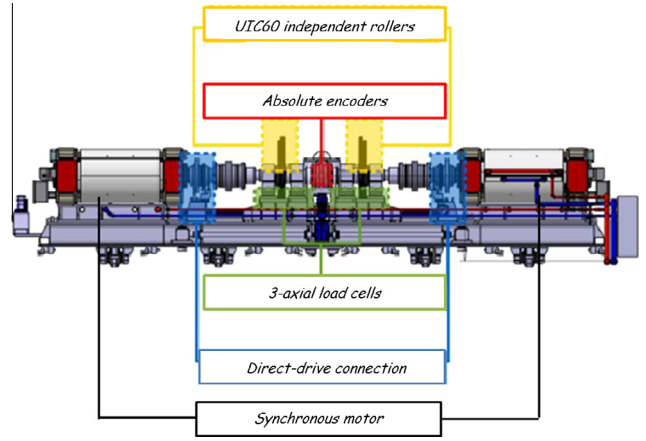

Fig. 9. Main roller-rig sensors.

Table 3
Roller-rig sensor characteristics.

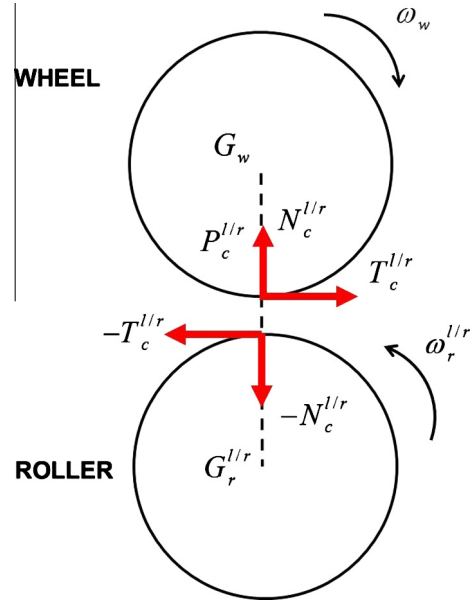| Sensor	Range	Resolution	Sensitivity	Passband
Absolute encoder	2π rad	$7 * 10^{-5}$ rad	$\pm0.01\%$ full scale	–
3-Axial load cells	±200 kN	7 N	$\pm0.1\%$ full scale	0.1 kHz

Fig. 10. Wheel-roller contact model.
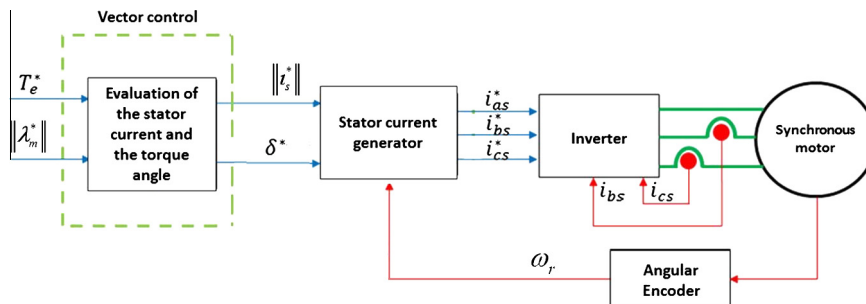

Fig. 8. Vector control block scheme.

contact forces $\mathbf{N^I_c}/\mathbf{r}$. Finally, the solution of the tangential contact problem is performed by means of the Kalker–Polach theory [29–31] to compute the tangential contact forces $\mathbf{T^I_c}/\mathbf{r}$. The contact model guarantees high accuracy and numerical efficiency; this way, the model can be implemented directly online inside the whole test-rig model.

3.2. The virtual railway vehicle model

The virtual railway vehicle model simulates the dynamical behaviour of the railway vehicle during a braking phase under degraded adhesion conditions. The model, designed for a real-time implementation, is composed of two parts: the 2D vehicle model and the 2D adhesion model. The inputs are the 4 estimated torques $\widehat{C}_s$ to be applied to the wheelsets while the outputs are the 4 simulated tangential contact forces T_{sim} and the 4 simulated wheel angular velocities ω_{ws}.

3.2.1. The virtual vehicle model

The 2D vehicle model of the considered railway vehicle (UIC-Z1 coach) is a simplified 2D multibody model of the longitudinal train dynamics (only 3 DOFs for each body are taken into account) [11]. The model (see Fig. 11) consists of a carbody, two bogies and four wheelsets, held by the primary and secondary suspensions. Starting from the estimated torques $\widehat{C}_s$, the model evaluates the kinematic variables of the 4 wheelsets v_{ws}, ω_{ws} and the 4 normal contact forces N_{cs} to be passed to the adhesion model and receives the 4 tangential contact forces T_{sim}.
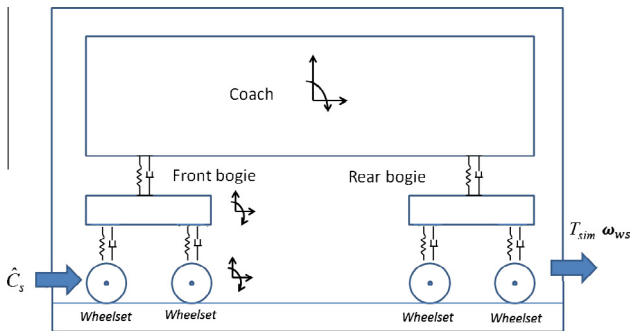
Fig. 11. The virtual railway vehicle model.

3.2.2. The adhesion model

The adhesion model has been especially developed to describe degraded adhesion conditions [17,32–34] and calculates, for all the 4 wheelset-rail pair, the tangential contact forces T_{sim} starting from the wheelset kinematic variables v_{ws}, ω_{ws} and the normal contact forces N_{cs} (see Fig. 12).

The main phenomena characterising the degraded adhesion are the large sliding occurring at the contact interface and, consequently, the high energy dissipation. Such a dissipation causes a cleaning effect on the contact surfaces and finally an adhesion recovery due to the removal of the external contaminants. When the specific dissipated energy W_{sp} is low the cleaning effect is almost absent, the contaminant level h does not change and the adhesion coefficient f is equal to its original value f_d in degraded adhesion conditions f_d. As the energy W_{sp} increases, the cleaning effect increases too, the contaminant level h becomes thinner and the adhesion coefficient f raises. In the end, for large values of W_{sp}, all the contaminant is removed (h is null) and the adhesion coefficient f reaches its maximum value f_r; the adhesion recovery due to the removal of external contaminants is now completed. At the same time if the energy dissipation begins to decrease, due for example to a lower sliding, the reverse process occurs (see Fig. 12).

Since the contaminant level h and its characteristics are usually totally unknown, it is usefull trying to experimentally correlate the adhesion coefficient f directly with the specific dissipated energy W_{sp}:

$$W_{sp} = T_{sim}e = fN_{cs}e \quad f = \frac{T_{sim}}{N_{cs}} \tag{11}$$

where the creepage e is defined as

$$e = \frac{s}{v_{ws}} = \frac{v_{ws} - r_w\omega_{ws}}{v_{ws}} \tag{12}$$

s is the sliding and r_w is the wheel radius. This way the specific dissipated energy W_{sp} can also be interpreted as the energy dissipated at the contact for unit of distance travelled by the railway vehicle.

To reproduce the qualitative trend previously described and to allow the adhesion coefficient to vary between the extreme values f_d and f_r, the following expression for f is proposed:

$$f = [1 - \lambda(W_{sp})]f_d + \lambda(W_{sp})f_r \tag{13}$$

where $\lambda(W_{sp})$ is an unknown transition function between degraded adhesion and adhesion recovery while the adhesion levels f_d, f_r can be evaluated according to [30,31] as a function of e, N_{cs} and the
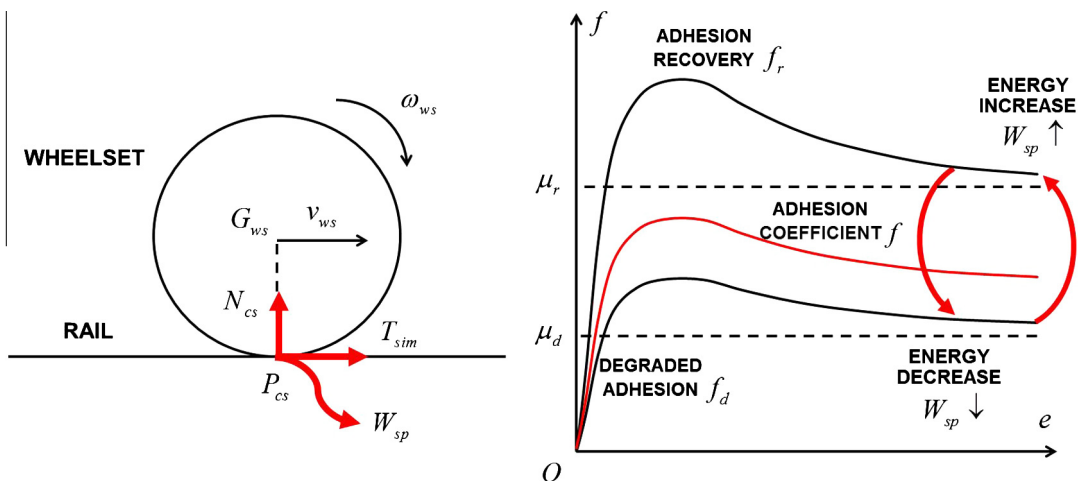
Fig. 12. The adhesion model.

track friction coefficients μ_d, μ_r (corresponding to degraded adhesion and full adhesion recovery, respectively). The function $\lambda(W_{sp})$ has to be positive and monotonous increasing; moreover the following boundary conditions are supposed to be verified: $\lambda(0) = 0$ and $\lambda(+\infty) = 1$.

This way, the authors suppose that the transition between degraded adhesion and adhesion recovery only depends on W_{sp}. This hypothesis is obviously only an approximation but, as it will be clearer in the next chapters, it well describes the adhesion behaviour. Initially, to catch the physical essence of the problem without introducing a large number of unmanageable and unmeasurable parameters, the authors have chosen the following simple expression for $\lambda(W_{sp})$:

$$\lambda(W_{sp}) = 1 - e^{-\tau W_{sp}} \tag{14}$$

where τ is now the only unknown parameter to be tuned on the base of the experimental data (in this case $\tau = 1.9 * 10^{-4}$ m/J) [13,16,20,35]. Finally the tangential forces $T_{sim} = fN_{cs}$ can be evaluated starting from the adhesion coefficient f calculated by solving the non-linear Eq. (13) (see Eq. (11) for the definition of W_{sp}) [36].

3.3. The controllers

The controllers have to reproduce on the roller-rig the dynamical behaviour of the virtual railway vehicle under degraded adhesion conditions in terms of angular velocities ω_w, applied torques C_s and, consequently, tangential contact forces $T_c^{l/r}$. The inputs of the controller are the simulated tangential forces T_{sim}, the simulated wheelset angular velocities ω_{ws}, the estimated wheel angular velocities $\widehat{\omega}_w$, the estimated motor torques $\widehat{C}_s$ and the roller angular velocities $\omega_r^{l/r}$. The outputs are the 8 roller control torques $u^{l/r}$.

The controller layout consists of 8 independent controllers (one for each roller) and makes use of a sliding mode strategy based on the dynamical equations of the roller rig; this way, it is possible to reduce the disturbance effects due to the system non-linearities and the parameter uncertainties [18,19]. The total control torques $u^{l/r}$ are defined as:

$$u^{l/r} = u_{cont}^{l/r} + u_{disc}^{l/r} + u_{diff}^{l/r} \tag{15}$$

where the continuous control part $u_{cont}^{l/r}$ is built starting from the approximated 1D models of wheelset and rollers and by supposing the slidings between the contact surfaces negligible (on the roller-rig the adhesion conditions are good, with a friction coefficient μ_{roll} equal to 0.3):

$$C_s = J_w \dot{\omega}_w - T_c^l r_w - T_c^r r_w$$
$$u^l = J_r \dot{\omega}_r^l - T_c^l r_w \quad u^r = J_r \dot{\omega}_r^r - T_c^r r_w$$
$$\omega_r^l = -\frac{r_w}{r_r} \omega_w \quad \dot{\omega}_r^l = -\frac{r_w}{r_r} \dot{\omega}_w \tag{16}$$
$$\omega_r^r = -\frac{r_w}{r_r} \omega_w \quad \dot{\omega}_r^r = -\frac{r_w}{r_r} \dot{\omega}_w$$

in which r_r, r_w are the roller and wheelset radii and J_r, J_w are their inertias. By removing T_c^l and T_c^r in Eq. (16), the following relation is obtained:

$$C_s - \frac{r_w}{r_r}(u^l + u^r) = J_{tot} \dot{\omega}_w \quad J_{tot} = J_w + 2\left(\frac{r_w}{r_r}\right)^2 J_r \tag{17}$$

where J_{tot} is the total inertia of the rollers and the wheelset reduced to the wheelset rotation axis. Subsequently the desired wheelset dynamics is considered

$$\widehat{C}_s = J_w \dot{\omega}_{ws} + T_{sim} r_w \tag{18}$$

together with the sliding surface $S = \omega_{ws} - \omega_w = 0$ and its time derivative $\dot{S} = \dot{\omega}_{ws} - \dot{\omega}_w$. If the torque estimation $\widehat{C}_s \simeq C_s$ is accurate enough, the sliding condition $\dot{S}$ can be obtained, starting from Eqs. (17) and (18), by taking

$$u = \frac{r_r}{r_w}\left[\left(1 - \frac{J_{tot}}{J_s}\right)\widehat{C}_s + \frac{J_{tot}}{J_s}T_{sim}r_w\right]$$
$$u^l = \frac{u}{2} \quad u^r = \frac{u}{2}. \tag{19}$$

On the other hand, $u_{disc}^{l/r}$ is the discontinuous control part related to the rejection of the disturbancies:

$$u_{disc}^l = u_{disc}^r = k\Re(\omega_{ws} - \widehat{\omega}_w). \tag{20}$$

The discontinuous controls $u_{disc}^{l/r}$ are characterised by the gain k and the function $\Re$ shown in Fig. 13 (the dead zone amplitude δ and the slope σ are control parameters to be tuned).

Finally, $u_{diff}^{l/r}$ is an auxiliary control part aimed at synchronising the roller angular velocities ω_r^l, ω_r^r:

$$u_{diff}^l = -k_d \aleph(\omega_r^l - \omega_r^r) \quad u_{diff}^r = k_d \aleph(\omega_r^l - \omega_r^r). \tag{21}$$

The function $\Re$ is reported in Fig. 13, while the parameters k_d, δ_d and σ_d have to be tuned. The controller performances will be evaluated by means of the angular velocity error
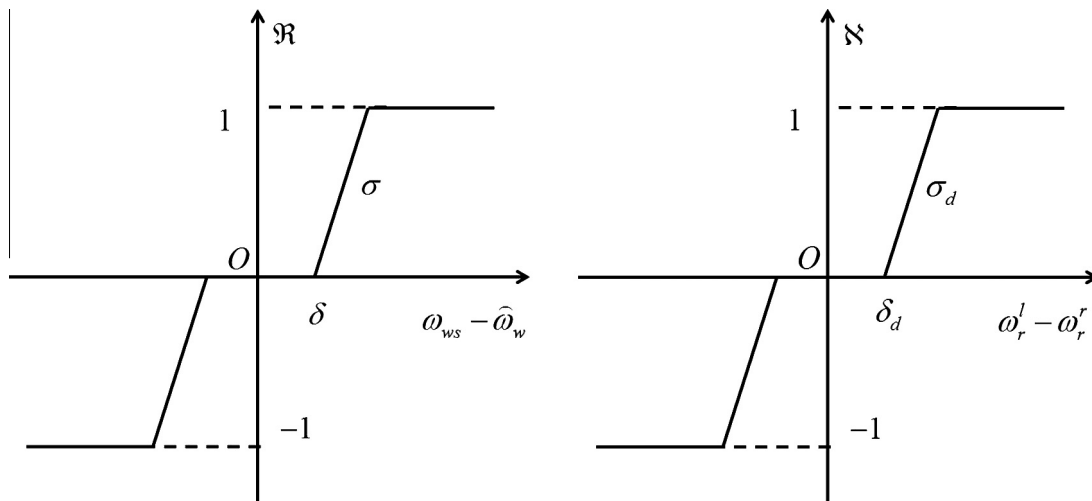

Fig. 13. Discontinuous and auxiliary control characteristics.

$e_\omega = \omega_{ws} - \omega_w$ and the torque estimation error $e_c = \widehat{C}_s - C_s$. Limited values of the previous errors e_ω, e_c assure a good estimation of the tangential contact forces $T_c^{l/r}$.

3.4. The torque estimators

The estimators aim at evaluating the wheelset angular velocities $\hat{\omega}_w$ and the torques applied to the wheelset $\widehat{C}_s$ starting from the roller angular velocities $\omega_r^{l/r}$ and the longitudinal reaction forces $T_{mis}^{l/r}$ on the roller supports. Since the slidings between wheelset and rollers can be neglected, the following estimations approximately hold:

$$\hat{\omega}_w = -\frac{r_r}{r_w}\frac{\omega_r^l + \omega_r^r}{2} \quad \dot{\hat{\omega}}_w = -\frac{r_r}{r_w}\frac{\dot{\omega}_r^l + \dot{\omega}_r^r}{2} \quad \widehat{T}_c^{l/r} = T_{mis}^{l/r}. \tag{22}$$

Of course, the derivative operation $\frac{d}{dt}$ has to be robust, taking into account the numerical noise affecting $\omega_r^{l/r}$. At this point, to estimate the motor torque applied to the wheelset, the estimator employes the simplified dynamical model of the wheelset:

$$\widehat{C}_s = J_w\dot{\hat{\omega}}_w - \widehat{T}_c^l r_w - \widehat{T}_c^r r_w. \tag{23}$$

It is worth noting that, in this kind of applications, the estimators have to be necessarily simple because they are thought for a real-time implementation and, at the same time, the physical characteristics of the railway vehicle on the roller-rig are generally unknown.

4. Experimental data

The HIL model performance have been validated by means of the comparison with the experimental data, provided by Trenitalia S. p. A. [13] and coming from on-track braking tests carried out in Velim (Czech Republic) with the coach UIC-Z1 [11]. The considered vehicle is equipped with a fully-working WSP system [12]. These

Table 4
Main characteristics of the braking test.

Parameter	Units	Value
Friction coefficient (degraded adhesion) μ_d	–	0.06
Friction coefficient (adhesion recovery) μ_r	–	0.28
Initial train velocity V	km/h	120
Nominal braking torque C	Nm	9500
Measurement sample time Δt_s	s	0.01

experimental tests have been carried out on a straight railway track. The wheel profile is the ORE S1002 (with a wheelset width d_w equal to 1.5 m) while the rail profile is the UIC60 (with a gauge d_r equal to 1.435 m and a laying angle α_p equal to 1/20 rad). The main characteristics of the braking test, considered as benchmark in this paper, are summarised in Table 4.

The value of the kinetic friction coefficient under degraded adhesion conditions μ_d depends on the test that has to be performed on the track; the degraded adhesion conditions are reproduced using a watery solution containing surface-active agents, e.g. a solution sprinkled by a specially provided nozzle on the first wheelset in the running direction. The surface-active agent concentration in the solution varies according to the type of test and the desired friction level. The value of the kinetic friction coefficient under full adhesion recovery μ_r corresponds to the classical kinetic friction coefficient under dry conditions.

Firstly the vehicle and wheelset velocities v^{sp}, $v_{wi}^{sp} = r_w\omega_{wi}^{sp}$ ($i = 1,\dots,4$) are taken into account (see Fig. 14). Both the WSP intervention and the adhesion recovery in the second part of the braking maneuver are clearly visible.

Secondly the slidings among the wheelsets and the rails have been considered: $s_i^{sp} = v^{sp} - r_w\omega_{wi}^{sp} = v^{sp} - v_{wi}^{sp}$ (see Figs. 17–20). However these physical quantities cannot be locally compared to each other because of the complexity and the chaoticity of the system due, for instance, to the presence of discontinuous and threshold elements like the WSP. To better evaluate the behaviour of s_i^{sp} from a global point of view, it is usefull to introduce the statistical means $\bar{s}_i^{sp}$ and the standard deviations Δ_i^{sp} of the considered variables:

$$\bar{s}_i^{sp} = \frac{1}{T_F - T_I} \int_{T_I}^{T_F} s_i^{sp} dt$$
$$\Delta_i^{sp} = \sqrt{\frac{1}{T_F - T_I} \int_{T_I}^{T_F} (s_i^{sp} - \bar{s}_i^{sp})^2 dt} \tag{24}$$

where T_I and T_F are respectively the initial and final times of the simulation (see Table 6).

5. The model validation

In this chapter the whole HIL architecture model is simulated and validated. More in detail, both the dynamical and the control performances of the system will be analysed. The main control and integration parameters are summarised in Table 5 (see the Section 3.3) [37].
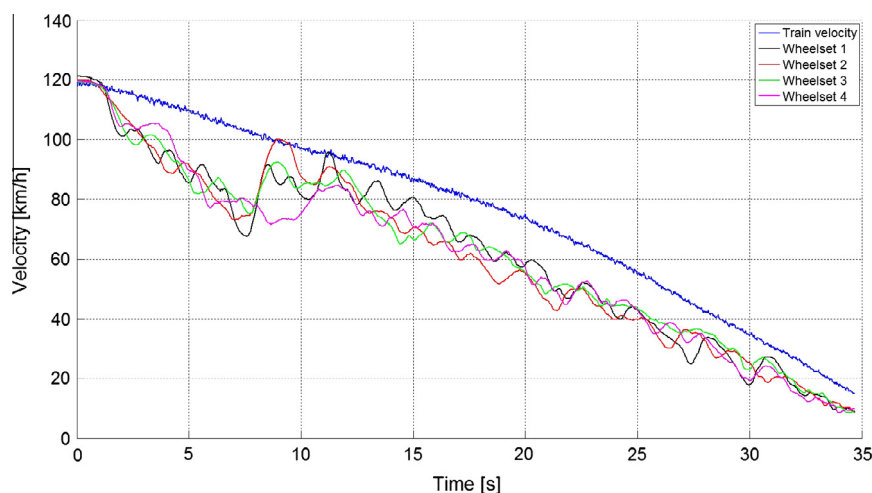

Fig. 14. Experimental vehicle and wheelset velocities v^{sp}, $v_{wi}^{sp} = r_w\omega_{wi}^{sp}$.

Table 5
Main control and integration parameters.

Parameter	Units	Value
Control gain k	Nm	$2 * 10^4$
Dead zone amplitude δ	rad/s	0.05
Control slope σ	Nm s/rad	10
Control gain k_d	Nm	$2 * 10^4$
Dead zone amplitude δ_d	rad/s	0.05
Control slope σ_d	Nm s/rad	10
Integration algorithm	–	ODE5, Dormand-Prince
Algorithm characteristics	–	Fixed step, V order
Integration stepsize Δt	s	10^{-4}

The simulated vehicle and wheelset velocities v_s, $v_{wsi} = r_w\omega_{wsi}$ are reported in Fig. 15). Figs. 14 and 15 highlight a good qualitative matching between experimental and simulated data, both concerning the WSP intervention and the adhesion recovery in the second part of the braking maneuver.

The direct comparison between the experimental and simulated train velocities v^{sp}, v_s is illustrated in Fig. 16 and shows also a good quantitative agreement between the considered quantities.

Subsequently, according to Section 4, the simulated slidings among wheelsets and rails $s_{si} = v_s - r_w\omega_{wsi} = v_s - v_{wsi}$ are taken into account and compared to the experimental ones s_i^{sp} (see Figs. 17–20).

The matching between experimental and simulated slidings is qualitatively good. However, since these physical quantities cannot be locally compared to each other because of the complexity and the chaoticity of the system, the statistical means $\bar{s}_{si}$ and the standard deviations Δ_{si} of the simulated slidings s_{si} are introduced (according to Eq. (24)) to better evaluate the global behaviour of analysed variables. The comparison between experimental
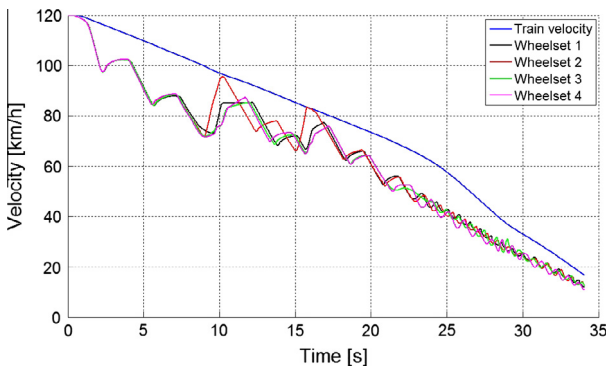

Fig. 15. Simulated vehicle and wheelset velocities v_s, $v_{wsi} = r_w\omega_{wsi}$.
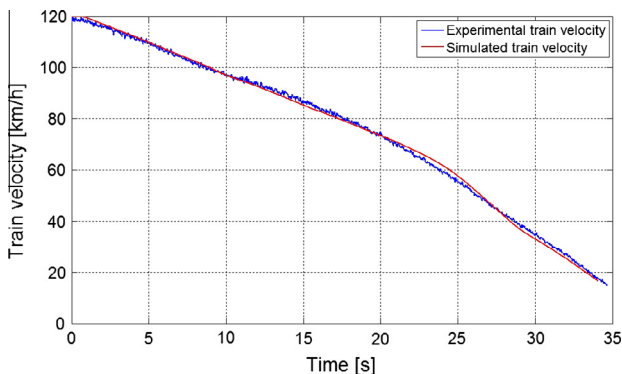

Fig. 16. Experimental and simulated train velocities v^{sp}, v_s.
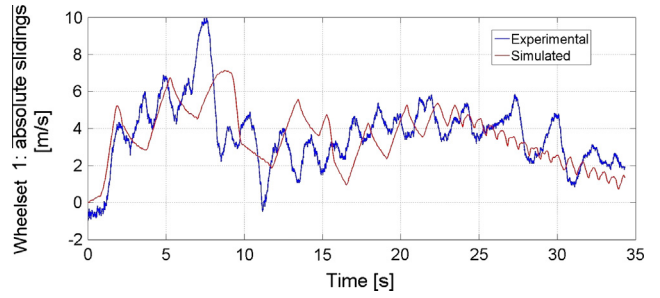

Fig. 17. Experimental and simulated train slidings s_1^{sp}, s_{s1} for the first wheelset.
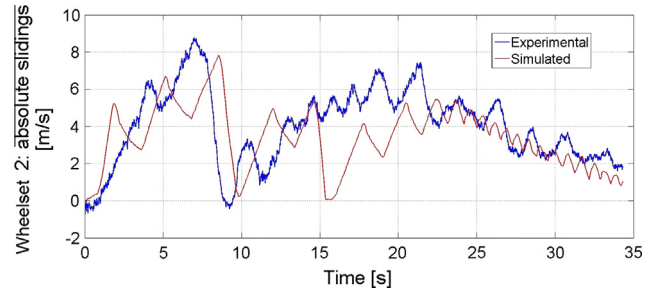

Fig. 18. Experimental and simulated train slidings s_2^{sp}, s_{s2} for the second wheelset.
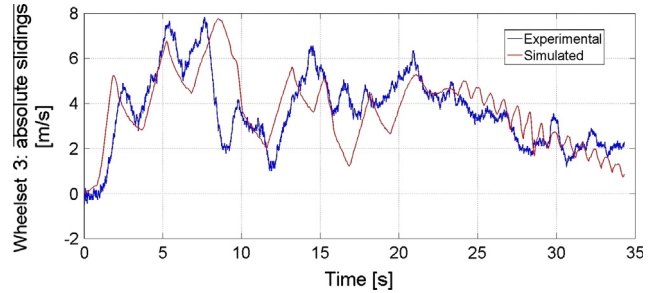

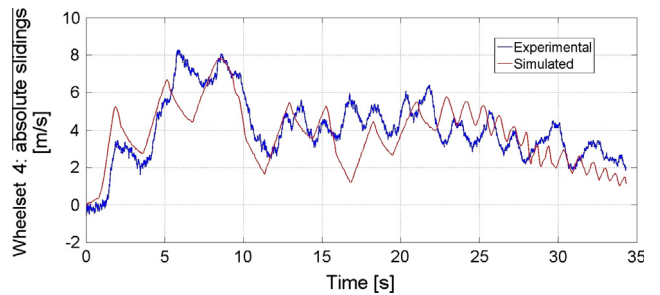**Fig. 19.** Experimental and simulated train slidings s_3^{sp}, s_{s3} for the third wheelset.

Fig. 20. Experimental and simulated train slidings s_4^{sp}, s_{s4} for the fourth wheelset.

$\bar{s}_i^{sp}$, Δ_i^{sp} and simulated $\bar{s}_{si}$, Δ_{si} statistical indices is reported in Table 6 and highlights also a good quantitative match between the studied quantities.

The controller performances are evaluated in terms of angular velocity error $e_\omega = \omega_{ws} - \omega_w$ and the torque estimation error $e_c = \widehat{C}_s - C_s$. Small values of the errors e_ω, e_c assure a good estimation of the tangential contact forces $T_c^{l/r}$. The time history of the angular velocity error e_ω is plotted in Fig. 21 and shows the control capabilty of stabilising the system and rejecting the disturbancies

Table 6
Experimental $\bar{s}_i^{sp}$, Δ_i^{sp} and simulated $\bar{s}_{si}$, Δ_{si} statistical indices.

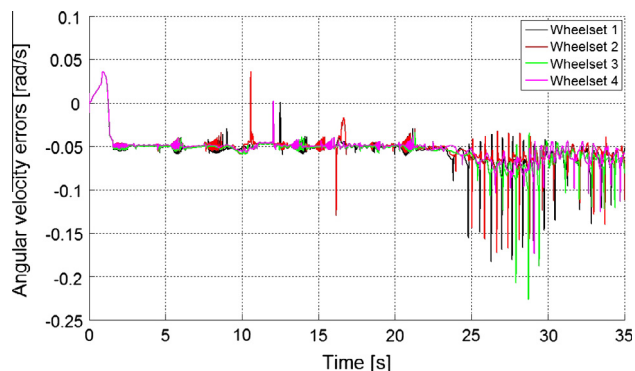| Wheelset	$\bar{s}_i^{sp}$ (km/h)	$\bar{s}_{si}$ (km/h)	Δ_i^{sp} (km/h)	Δ_{si} (km/h)
Wheelset 1	13.08	12.82	6.45	6.56
Wheelset 2	13.36	12.88	7.25	6.95
Wheelset 3	13.09	13.32	5.92	5.70
Wheelset 4	13.52	13.59	6.22	5.82

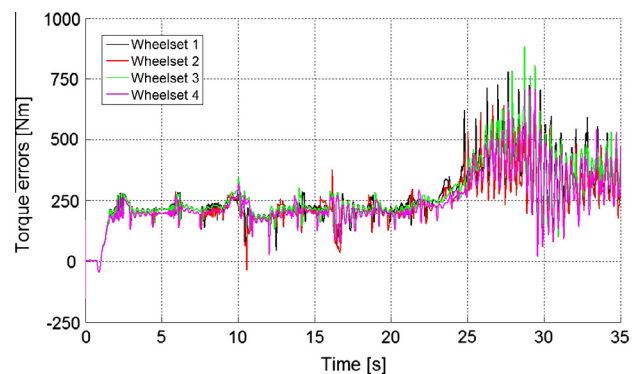**Fig. 21.** Angular velocity error $e_\omega = \omega_{ws} - \omega_w$.

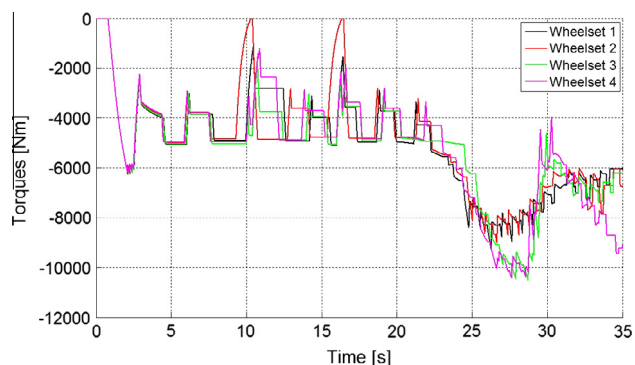**Fig. 22.** Torque estimation error $e_c = \hat{C}_s - C_s$.

Fig. 23. Torque applied to the wheelset C_s.

produced by the initial transient and the adhesion recovery in the second phase of the braking maneuvre.

The torque estimation error $e_c = \hat{C}_s - C_s$ and the real torques applied to the wheelset C_s are reported respectively in Figs. 22 and 23. Also in this case the controllers turn out to be effective in reproducing the real torques applied to the wheelsets of the vehicle.

Finally, the result analysis highlights the control capability of reproducing on the roller-rig a generic wheel-rail degraded adhesion pattern calculated by the reference virtual railway vehicle model (in terms of angular velocities ω_w, applied torques on the wheelsets C_s and, consequently, in terms of tangential efforts $T_c^{l/r}$ exchanged between the wheelsets and the rails).

6. Conclusions and further developments

In this paper the authors presented an innovative Hardware In the Loop (HIL) approach for testing braking on board subsystems on full-scale roller-rigs. The new approach permits the reproduction on the roller-rig of a generic wheel-rail adhesion pattern and, in particular of, degraded adhesion conditions. The proposed approach has been validated through the experimental data provided by Trenitalia and highlighted good performance in reproducing on the roller-rig the complex behaviour of the degraded adhesion during the braking of a railway vehicle.

The innovative full-scale roller-rig of the Firenze-Osmannoro research facility represents an important improvement for the railway industries; particularly, the reduction of the expensive on-track tests (rent of vehicle and railway lines) and the possibility to test several on board subsystems on a roller-rig (with good adhesion conditions or degraded ones) are the main advantages of the system.

The future developments of this research activity will concern the real implementation of the controller strategy and the virtual vehicle model on the Firenze-Osmannoro roller-rig: firstly, used as further validation of the proposed HIL approach through experimental tests performed directly on the roller-rig, and, finally, as complete HIL system especially developed for the testing of the on board subsystems (WSP, antiskid, etc.).

References

[1] Jaschinki A, Chollet H, Iwnicki S. The application of the roller rigs to railway vehicle dynamics. Veh Syst Dynam 1999;31:325–44.
[2] Dukkipati R. A parametric study of the lateral stability of a railway bogie on a roller rig. Proc Inst Mech Eng Part F 1999;213:39–47.
[3] Ahn K, Park J, Ryew S. The construction of a full-scale wheel/rail roller rig in Korea. In: Proceedings of the IEEE international conference on automation science and engineering (CASE); 2012. p. 802–3.
[4] Lee N, Kang C, Lee W, Dongen T. Roller rig tests of a semi-active suspension system for a railway vehicle. In: Proceedings of the IEEE international conference on control, automation and systems (ICCAS); 2012. p. 117–22.
[5] Zhang W, Chen J, Wu X, Jin X. Wheel/rail adhesion and analysis by using full scale roller rig. Wear 2002;253:82–8.
[6] Ignesti M, Malvezzi M, Marini L, Meli E, Rindi A. Development of a wear model for the prediction of wheel and rail profile evolution in railway systems. Wear 2012;284–285:1–17.
[7] Innocenti A, Marini L, Meli E, Pallini G, Rindi A. Development of a wear model for the analysis of complex railway networks. Wear 2013;309:174–91.
[8] Malvezzi M, Allotta B, Pugi L, Rindi A. Control of a full scale locomotive roller rig for the simulation of wheel sliding. In: Proceedings of the IEEE/ASME conference on mechatronics; 2007. p. 1–6.
[9] UNI-EN. Railway applications, braking-wheel sliding protection. UNI-EN 15595; 2009.
[10] Official site of mathworks, Natick, MA; 2013. <http://www.mathworks.com>.
[11] Trenitalia SpA. UIC-Z1 coach. Internal report of Trenitalia; 2000.
[12] Trenitalia SpA. WSP system. Internal report of Trenitalia; 2005.
[13] Trenitalia SpA. On-track braking tests. Internal report of Trenitalia; 2006.
[14] Trenitalia SpA. Full-scale roller-rig: technical documentation. Internal report of Trenitalia; 2011.
[15] SICME Motori. IPM synchronous motor datasheet. Internal report of SICME Motori; 2010.

[16] Allotta B, Conti R, Malvezzi M, Meli E, Pugi L, Ridolfi A. Numerical simulation of a HIL full scale roller-rig model to reproduce degraded adhesion conditions in railway applications. In: Proceedings of the ECCOMAS 2012 congress; 2012.

[17] Allotta B, Meli E, Ridolfi A, Rindi A. Development of an innovative wheel–rail contact model for the analysis of degraded adhesion in railway systems. Tribology International 2013;69:128–40.

[18] Sontag ED. Mathematical control theory. New York: Springer-Verlag; 1998.

[19] Khalil HK. Nonlinear systems. United States: Prentice Hall; 2002.

[20] Conti R, Meli E, Pugi L, Malvezzi M, Bartolini F, Allotta B, et al. A numerical model of a HIL scaled roller rig for simulation of wheel-rail degraded adhesion condition. Veh Syst Dynam 2012;50:775–804.

[21] Malvezzi M, Meli E, Rindi A, Falomi S. Determination of wheel-rail contact points with semianalytic method. Multibody Syst Dynam 2008;20:327–58.

[22] Malvezzi M, Meli E, Falomi S. Multibody modeling of railway vehicles: innovative algorithms for the detection of wheelrail contact points. Wear 2011;271:453–61.

[23] Magheri S, Malvezzi M, Meli E, Falomi S, Rindi A. An innovative wheelrail contact model for multibody applications. Wear 2011;271:462–71.

[24] Ignesti M, Innocenti A, Marini L, Meli E, Rindi A. Development of a model for the simultaneous analysis of wheel and rail wear in railway systems. Multibody System dynamics 2013. http://dx.doi.org/10.1007/s11044-013-9360-0.

[25] Krishnan R. Permanent magnet synchronous and brushless DC motor drives. CRC Press, Taylor and Francis group; 2010.

[26] Vagati A, Pellegrino G, Guglielmi P. Design tradeoff between constant power speed range, uncontrolled generator operation and rated current of IPM motor drives. IEEE Trans Ind Appl 2011;47:1995–2003.

[27] Li S, Xia C, Zhou X. Disturbance rejection control method for permanent magnet synchronous motor speed-regulation system. Mechatronics 2012;22:706–14.

[28] Vu NT, Choi HH, Jung J. Certainty equivalence adaptive speed controller for permanent magnet synchronous motor. Mechatronics 2012;22:811–8.

[29] Kalker JJ. Three-dimensional elastic bodies in rolling contact. Norwell, MA: Kluwer Academic Publishers; 1990.

[30] Polach O. Creep forces in simulations of traction vehicles running on adhesion limit. Wear 2005;258:992–1000.

[31] Polach O. A fast wheel-rail forces calculation computer code. Veh Syst Dynam 1999;33:728–39.

[32] Blau PJ. Embedding wear models into friction models. Tribol Lett 2009;34:75–9.

[33] Boiteux M. Le probleme de l'adherence en freinage. Rev Gen Chemins 1986:59–72.

[34] Voltr P, Lata M, Cerny O. Measuring of wheel-rail adhesion characteristics at a test stand. In: Proceedings of XVIII conference on engineering mechanics; 2012.

[35] Nocedal J, Wright S. Numerical optimization. Springer series in operation research, Berlin, Germany; 1999.

[36] Kelley C. Iterative methods for linear and nonlinear equations. Philadelphia, PA: SIAM; 1995.

[37] Shampine L, Reichelt M. The Matlab ODE suite. SIAM J Sci Comput 1997;18:1–22.